

## Multiphase-field simulation of austenite reversion in medium-Mn steels

Yan Ma<sup>1,3</sup>, Rui Zheng<sup>1</sup>, Ziyuan Gao<sup>1</sup>, Ulrich Krupp<sup>1</sup>, Hai-wen Luo<sup>2</sup>, Wenwen Song<sup>1</sup>,  
and Wolfgang Bleck<sup>1</sup>

1) Steel Institute (IEHK), RWTH Aachen University, Intzestraße 1, 52072 Aachen, Germany

2) Department of Ferrous Metallurgy, University of Science and Technology Beijing, Beijing 100083, China

3) Max-Planck-Institut für Eisenforschung GmbH (MPIE), Max-Planck-Straße 1, 40237 Düsseldorf, Germany

(Received: 13 January 2020; revised: 17 March 2020; accepted: 22 March 2020)

**Abstract:** Medium-Mn steels have attracted immense attention for automotive applications owing to their outstanding combination of high strength and superior ductility. This steel class is generally characterized by an ultrafine-grained duplex microstructure consisting of ferrite and a large amount of austenite. Such a unique microstructure is processed by intercritical annealing, where austenite reversion occurs in a fine martensitic matrix. In the present study, austenite reversion in a medium-Mn alloy was simulated by the multiphase-field approach using the commercial software MICRESS<sup>®</sup> coupled with the thermodynamic database TCFe8 and the kinetic database MOBFE2. In particular, a faceted anisotropy model was incorporated to replicate the lamellar morphology of reversed austenite. The simulated microstructural morphology and phase transformation kinetics (indicated by the amount of phase) concurred well with experimental observations by scanning electron microscopy and *in situ* synchrotron high-energy X-ray diffraction, respectively.

**Keywords:** medium-Mn steels; intercritical annealing; austenite reversion; phase-field simulation; faceted anisotropy model

### 1. Introduction

Since the 2000s, medium-Mn steels containing 3wt%–12wt% manganese have drawn immense attention due to their attractive mechanical properties (product of tensile strength and total elongation up to ~70 GPa) [1–3]. This steel class has been considered as a major contender of the third-generation advanced high-strength steels for future automotive applications [4–6]. In general, such steels are processed by intercritical annealing, where austenite reversion takes place in a fine martensitic matrix [7]. As a result, medium-Mn steels reveal an ultrafine-grained duplex microstructure consisting of ferrite and a large amount of reversed austenite (20vol%–60vol%) [5]. Numerous studies have emphasized the effects of heat treatment parameters (e.g., annealing temperature [8–11], annealing time [12–13], heating rate prior to isothermal holding [14], cooling rate after isothermal holding [15–16], primary austenitization [17–18], etc.) on microstructures and mechanical properties in medium-Mn steels. It is appreciated that microstructures and mechanical properties in this steel class can be adjusted by heat treatment in a very wide range.

Computational modeling of microstructure evolution in

materials science has been rapidly developed in recent years. Phase-field simulation is particularly appealing because it provides a visual impression of microstructure evolution during processing. Such a simulation approach is capable of considering the synergetic contribution of various thermodynamic driving forces (e.g., bulk free energy, interfacial energy, and stored elastic energy, etc.) to microstructure evolution [19–21]. Many attempts have been made to simulate microstructure evolution during austenite decompositions in steels [22], such as pearlite reaction [23], Widmanstätten ferrite growth [7], martensitic transformation [6], and bainitic transformation [24–25]. The phase-field method has been proven to be a competent tool to depict the complex microstructure evolution and disentangle the underlying phase transformation mechanisms in steels. To better understand the austenite reversion mechanisms in medium-Mn steels, a multiphase-field model has been built up in the present study. The well calibrated model could be applied to simulate the microstructure evolution under various heat treatment conditions as a guidance for heat treatment adjustment to achieve targeted microstructures and mechanical properties in this steel class.

The present work aims at establishing a multiphase-field

model for simulating austenite reversion in a medium-Mn alloy Fe–12Mn–3Al (in wt%). The two-dimensional microstructure simulation is conducted using the commercial phase-field software MICRESS<sup>®</sup> (MICROstructure Evolution Simulation) coupled with the thermodynamic database TCFE8 and the kinetic database MOBFE2 in the software Thermo-Calc. Moreover, a faceted anisotropy model was incorporated in the model to replicate the lamellar morphology of reversed austenite. In the simulation, austenite reversion from martensite is assumed to be predominated by the diffusion-controlled transformation. The simulated microstructural morphology and phase transformation kinetics (indicated by phase fraction) are compared with the experimental observations. Manganese and aluminum redistribution across the austenite–ferrite interfaces is further investigated and discussed.

## 2. Simulation and experimental methods

### 2.1. Multiphase-field model

In the literature, it was reported that the austenite reversion in medium-Mn steels is dominated by local equilibrium partitioning of substitutional elements (mainly manganese) [26]. Therefore, in the present study, a multiphase-field model was built up for a simplified Fe–Mn–Al ternary alloy system. The nominal chemical composition was Fe–12Mn–3Al (in wt%) in the simulation. In this case, the trivial effect of interstitial carbon on austenite reversion was neglected, which was reported to play a role in the very early stage of austenite growth under non-partitioning local equilibrium mode due to the fast diffusivity of carbon in ferrite [27].

In the multiphase-field model, the kinetics of the austenite reversion can be described by phase-field order parameters  $\phi_i(\vec{x}, t)$ . Such parameters describe the temporospatial state in space  $\vec{x}$  and at time  $t$  of microstructure constituent, e.g., grain  $i$  ( $i = 1, \dots, N$ ), assuming a value of 1 inside grain  $i$  and 0 outside of the grain. At the interface between two grains (e.g., grain  $i$  and grain  $j$ ), there is a continuous change in the corresponding phase-field order parameters between 0 and 1, where,  $0 < \phi_i < 1$ ,  $0 < \phi_j < 1$ , and  $\phi_i + \phi_j = 1$ . In general,  $\sum_i^N \phi_i(\vec{x}, t) = 1$  holds at each position,  $\vec{x}$ , in the simulation domain with a total number of  $N$  grains. The time evolution of the phase-field order parameter is given by pairwise interactions with neighboring grains:

$$\frac{d\phi_i}{dt} = \sum_{i \neq j} \mu_{ij} \left[ \sigma_{ij} \left( \phi_i \nabla^2 \phi_j - \phi_j \nabla^2 \phi_i + \frac{\pi^2}{2\eta_{ij}^2} (\phi_i - \phi_j) \right) + \frac{\pi}{\eta_{ij}} \sqrt{\phi_i \phi_j} \Delta G_{ij} \right] \quad (1)$$

where  $\mu_{ij}$  is the interface mobility,  $\sigma_{ij}$  is the effective anisotropic interface energy,  $\eta_{ij}$  is the thickness of the interface, and  $\Delta G_{ij}$  is the free energy difference of two interacting

grains  $i$  and  $j$ .

In such an expression, the evolution of the phase-field order parameter is driven by interface curvature contribution (the first term of Eq. (1)) and thermodynamic driving force (the second term of Eq. (1)). The thermodynamic driving force is a function of the local chemical composition, and the phase-field order parameter is further incorporated with the diffusion equations. For multicomponent systems (e.g., here Fe–Mn–Al ternary alloy system), the time dependence of the local content  $\vec{c}$  is given by:

$$\frac{\partial \vec{c}}{\partial t} = \nabla \cdot \sum_{i=1}^N \phi_i D_i \nabla \vec{c}_i \quad (2)$$

where  $D_i$  is the multicomponent diffusion coefficient matrix for phase  $i$ . Such diffusion coefficients were directly coupled with the kinetic database MOBFE2 in the software Thermo-Calc. Moreover, a factor of five was implemented in the present work for enhanced diffusion of manganese and aluminum in martensite (viz., five times higher diffusivity in martensite compared with ferrite), since the defects stored in martensite can facilitate elemental partitioning [26,28].

Thermodynamic interactions between  $\alpha'$ -martensite matrix and reversed  $\gamma$ -austenite were coupled with the thermodynamic database TCFE8 using the software Thermo-Calc. The direct implementation of  $\alpha'$ -martensite in phase-field simulation is impossible because a non-equilibrium phase (here  $\alpha'$ -martensite) is not included in the thermodynamic database. In practice,  $\alpha'$ -martensite was treated as body-centered cubic ferrite ( $\alpha$ ) in the simulation. Additionally, the driving force “offset” option was employed to describe martensite in the sense of ‘metastable’, which allows a shift in Gibbs energy curve of  $\alpha$ -ferrite, denoted as the offset energy for phase interaction  $\alpha/\gamma$  in the software MICRESS<sup>®</sup>. The offset energy was set to be  $-10 \text{ J/cm}^3$  in the present work. Such modification implies that  $\alpha'$ -martensite is considered as  $\alpha$ -ferrite in the phase-field simulation, albeit it is thermodynamically less stable compared with  $\alpha$ -ferrite. For simplicity, hereafter,  $\alpha'$ -martensite is denoted as  $\alpha$ -ferrite in the simulation.

To describe the anisotropic growth of reversed austenite according to its lamellar morphology, a faceted anisotropy model [29] was employed in the present simulation. Such a model allows describing crystallographic orientation-dependent physical properties, e.g., interfacial energy and interfacial mobility [29]. For each facet type, the interfacial energy  $\sigma_{ij}$  is expressed as:

$$\sigma_{ij} = \sigma_0 \cdot k_{st}^2 \cdot (k_{st}^2 \cdot \cos \theta^2 + \sin \theta^2)^{-\frac{3}{2}} \quad (3)$$

Where  $\sigma_0$  is the interfacial energy coefficient between two phases, and it was assumed to be  $2.0 \times 10^{-5} \text{ J/cm}^2$  for all interfaces in the present simulation [25];  $k_{st}$  represents the static anisotropy, and  $\theta$  indicates the misorientation of the normal vector of the  $\alpha/\gamma$  interface to the normal vector of the nearest facet. The interfacial mobility  $\mu_{ij}$  is calculated as:

$$\mu_{ij} = \mu_0 \left[ k_{\text{kin}} + (1 - k_{\text{kin}}) \cdot \tan\left(\frac{\kappa}{\tan \theta}\right) \cdot \frac{\tan \theta}{\kappa} \right] \quad (4)$$

where  $\mu_0$  defines the interfacial kinetic coefficient between two adjacent grains (here austenite and ferrite), indicating the interface mobility, which is an adjustable parameter to replicate the experimental kinetics;  $k_{\text{kin}}$  is kinetics anisotropy coefficient; and  $\kappa$  defines the broadness of the anisotropy with a value between 0 and 1. The morphology of grains is thus controlled by the value of  $k_{\text{kin}}$ .  $k_{\text{kin}} = 0$  represents the maximal anisotropic growth of the grains, while  $k_{\text{kin}} = 1$  indicates isotropic growth. Smaller  $k_{\text{kin}}$  values give rise to faster growth in the lengthening direction and slower growth in the widening direction. To replicate the experimental observation of microstructure morphology,  $\kappa = 0.3$ ,  $k_{\text{st}} = 0.03$ , and  $k_{\text{kin}} = 0.9$  were specified in the current simulation. Moreover, the set of normal vectors  $\{10\ 2\ 1\}$  was selected.

In order to replicate the overall austenite reversion kinetics, a simulation domain was set to be 500 grids by 325 grids with an ultrafine grid size of 5 nm (the corresponding domain size: 2500 nm  $\times$  1625 nm). The simulation was conducted under a gradient boundary condition and an insulation boundary condition for phase field and content field, respectively. The thickness of an interface was defined to be five times of the grid size in the simulation (i.e., 25 nm). The input file of the initial microstructure (that is lath martensite) was generated by the software GIMP (GNU Image Manipulation Program) based on a micrographic image of the homogenized medium-Mn steel Fe–12Mn–3Al–0.05C (in wt%), as shown in Fig. 1. Such a virtual microstructure was then converted into ASCII format as the input file in the software MICRESS®.

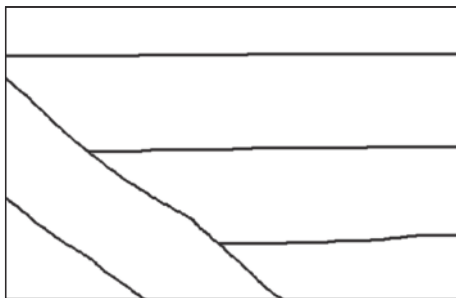


**Fig. 1.** Initial microstructure generated using the software GIMP based on a micrographic image of the homogenized medium-Mn steel; the domain geometry is 500 grids  $\times$  325 grids, and the corresponding domain size is 2500 nm  $\times$  1625 nm.

For austenite nucleation, a seed undercooling model was employed. In this case, the nucleation occurred when the local undercooling at a nucleus position exceeded a critical value, i.e., minimal undercooling 20 K. The nucleation sites of austenite were set to be at  $\alpha/\alpha$  interfaces and triple junctions based on the experimental micrographs. Moreover, the shield effect was used to control the nucleation distribution

over distance and time, replicating the qualitative metallography observations. A shield time of 1000 and 20 s was applied for nucleation at  $\alpha/\alpha$  interfaces and triple junctions, respectively. A shield distance was set to be 500 nm.

## 2.2. Experimental methods

A low-carbon medium-Mn steel with the nominal chemical composition of Fe–12Mn–3Al–0.05C (in wt%) was investigated in the current study. The  $A_{e1}$  and  $A_{e3}$  temperatures were predicted by the software ThermoCalc with the TCFE8 database to be approximately 490 and 755°C, respectively ( $A_{e1}$ : boundary temperature between three-phase field ( $\gamma + \alpha + \text{carbide}$ ) and two-phase field ( $\gamma + \alpha$ ) in equilibrium condition;  $A_{e3}$ : boundary temperature between two-phase field ( $\gamma + \alpha$ ) and single-phase field  $\gamma$  in equilibrium condition). The laboratory-processed alloy was cast into an ingot and forged. Subsequently, hot rolling was performed at 1150°C and the thickness of the sheet was reduced from 40 to 2.5 mm. Homogenization treatment was then conducted at 1100°C for 2 h, followed by water quenching to room temperature [30]. The microstructure of the homogenized samples was characterized by a Zeiss Sigma field-emission scanning electron microscope (SEM). The samples were prepared by mechanical grinding and polishing, followed by electropolishing and etching with 3wt% nital.

*In situ* synchrotron high-energy X-ray diffraction (HEXRD) was employed to measure the amount of the reversed austenite during intercritical annealing. The HEXRD experiment was performed at the Powder Diffraction and Total Scattering beamline P02.1 of PETRA III at Deutsches Elektronen-Synchrotron (DESY) in Hamburg, Germany [31]. This beamline provides a monochromatic X-ray with a wavelength of  $\sim 0.0207$  nm. A ceramic furnace attached to the synchrotron X-ray beamline was placed between the incident beam and the two-dimensional detector for conducting intercritical annealing. The geometry of the sample was 0.8 mm in diameter and 10 mm in length. The size of the incident beam was 1.0 mm  $\times$  1.0 mm, enabling full illumination of the sample along the radial direction. The intercritical annealing was carried out at 550°C for 10 h, with a heating rate of  $\sim 50^\circ\text{C/s}$ . Such a low annealing temperature can result in a strong enrichment of manganese in austenite and a high stacking fault energy of austenite ( $\sim 25$  mJ/m<sup>2</sup>), which may trigger the twinning-induced plasticity effect during deformation at room temperature [11,32]. The two-dimensional Debye–Scherrer patterns were recorded by a fast area detector PerkinElmer XRD1621 with a frequency of one exposure every second and exposure time of one second. The diffraction patterns were integrated using the Fit2D software [33]. The phase fraction was analyzed by the Rietveld refinement method using the Materials Analysis Using Diffraction (MAUD) software [34]. The detailed analysis procedures were documented elsewhere [35].

### 3. Results and discussion

#### 3.1. Microstructure evolution

The initial microstructure was lath martensite, as illustrated in Fig. 1. In this state, a homogeneous distribution of manganese and aluminum was assumed. Austenite reversion was simulated during the isothermal intercritical annealing at 550°C. Figs. 2(a)–2(d) show the simulated manganese content evolution as a function of intercritical annealing durations, i.e., 1, 4, 6, and 10 h, revealing the progress of the austenite growth during intercritical annealing. The obvious contrast in color indicated redistribution of manganese between reversed austenite and ferrite during austenite reversion. The detailed elemental partitioning behavior of manganese and aluminum across the phase boundaries will be presented in Section 3.3. The corresponding phase map is displayed in Fig. 2(e) after intercritical annealing for 10 h. The reversed austenite was enriched in manganese (indicated by orange color), while manganese was depleted in ferrite (indicated by bluish color).

By employing the faceted anisotropy model (Eqs. (3) and (4)), the reversed austenite grains possessed a rapid lengthening rate yet a limited growth rate in width direction during austenite reversion. As a consequence, the reversed austenite grains showed a lamellar morphology in the phase-field simulation after intercritical annealing for 10 h (Fig. 2(e)), which concurred well the microstructure observed by SEM (Fig. 2(f)). Moreover, the lamellar width and length of the reversed austenite were  $\sim 100$  nm and in the range of 400 to 700 nm, respectively. These numbers are in good agreement with the experimental observations.

#### 3.2. Austenite reversion kinetics

The predicted austenite reversion kinetics is shown in Fig. 3 (black curves). The simulation implies that austenite reversion started after a short incubation period ( $\sim 1100$  s) during the isothermal intercritical annealing at 550°C. Subsequently, the amount of reversed austenite increased progressively, and it reached  $\sim 18$  vol% after annealing for 10 h. The amount of reversed austenite and ferrite measured by

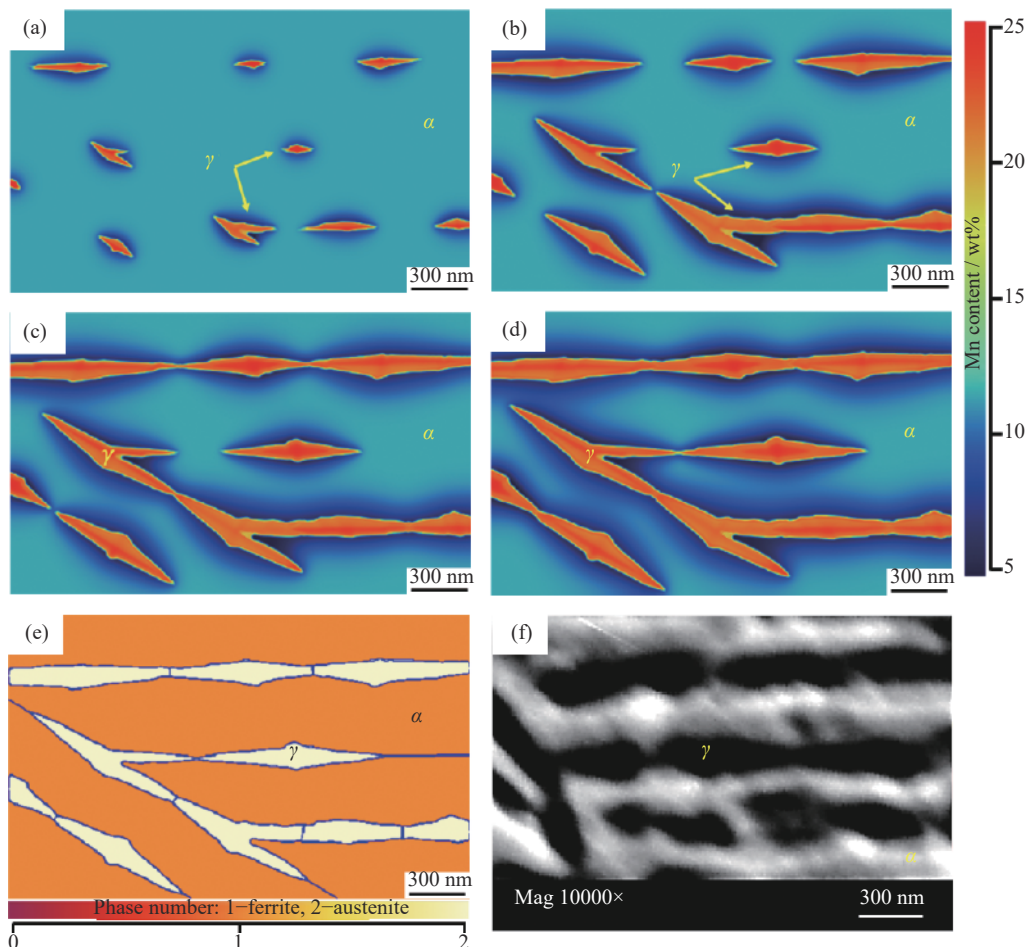
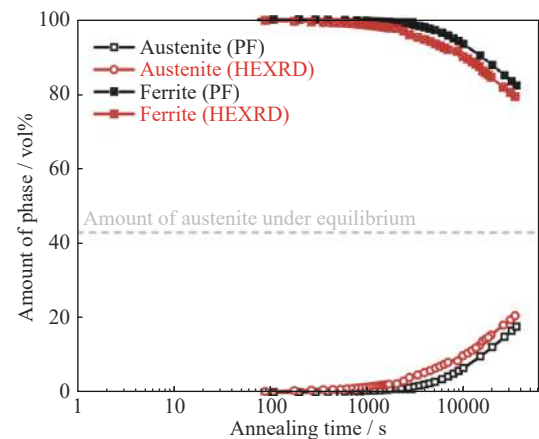


Fig. 2. Evolution of manganese content in the phase-field simulation during austenite reversion at 550°C for (a) 1, (b) 4, (c) 6, and (d) 10 h; (e) simulated phase map after intercritical annealing for 10 h; (f) scanning electron microscopy image of medium-Mn steel Fe–12Mn–3Al–0.05C (in wt%) intercritically annealed at 550°C for 10 h.  $\alpha$  stands for ferrite and  $\gamma$  for austenite.

HEXRD during intercritical annealing of medium-Mn steel Fe-12Mn-3Al-0.05C (in wt%) is also displayed in Fig. 3 (red curves). The phase-field simulation demonstrates a similar kinetic trend as the experimental observation, despite a small deviation of the amount of reversed austenite in simulation from that in experimental measurement. Such discrepancy was about 3vol% after intercritical annealing for 10 h. The kinetic difference between the simulation and experimental measurement could be attributed to the following facts: (1) In the phase-field simulation, the incorporated kinetic parameters, such as diffusivity and interfacial mobility, can strongly affect phase transformation kinetics [25]; therefore, appropriate input kinetic data for specific cases are supposed to be further justified in the future simulation with experimental support. (2) In the experiment, heating to isothermal intercritical-annealing temperature was also involved (with a heating rate of  $\sim 50^\circ\text{C}/\text{s}$ ), yet such process was not included in the simulation; thus, a bit longer incubation period might be observed in the simulation, which may lead to slightly slower reversion kinetics compared with the experiment. (3) In the experiment, the investigated material contains a small amount of carbon ( $\sim 0.05\text{wt}\%$ ), and rapid carbon diffusion in ferrite may contribute to fast growth kinetics of austenite under non-partitioning local equilibrium mode in the very early stage [27], which was not considered in the phase-field simulation.

### 3.3. Elemental partitioning behavior across austenite – ferrite phase boundaries

The evolution of the solute element partitioning across  $\alpha/\gamma$  phase boundaries was predicted as a function of intercritical-annealing time, as illustrated in Fig. 4. The result revealed that the content of manganese and aluminum in the reversed



**Fig. 3.** Evolution of the austenite and ferrite during intercritical annealing at  $550^\circ\text{C}$  predicted by phase-field (PF) simulation and measured by synchrotron high-energy X-ray diffraction (HEXRD). The equilibrium amount of austenite was predicted by the software Thermo-Calc with the database TCFe8.

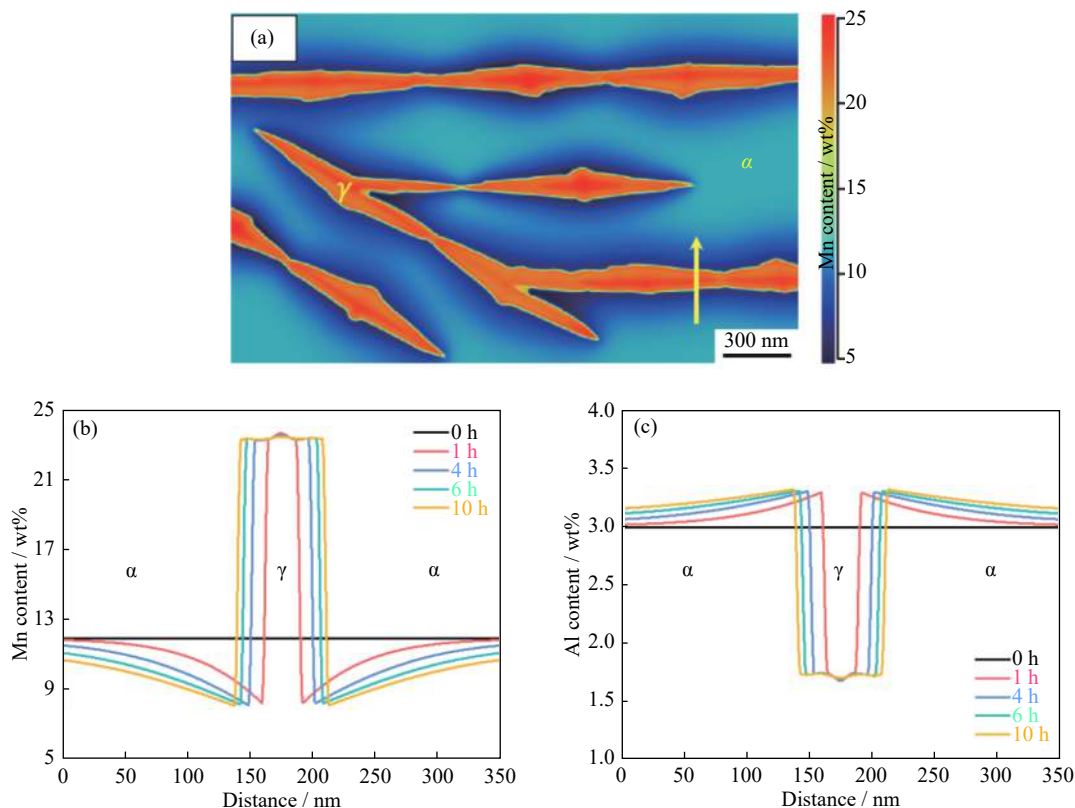


**Fig. 4.** (a) Predicted manganese content map after intercritical annealing at  $550^\circ\text{C}$  for 10 h; (b) manganese and (c) aluminum content profiles across the austenite–ferrite phase boundaries (indicated by the arrow in (a)) as a function of intercritical-annealing time.

austenite was nearly a constant value, which was independent on the intercritical-annealing time. Thus, austenite growth was predominately controlled by manganese diffusion through ferrite towards austenite–ferrite interfaces under partitioning local equilibrium and also by the mobility of the hetero-interfaces, which agreed well with the literature [26]. The latter aspect was indicated by the manganese gradient in ferrite ahead of the advancing interfaces. This chemical gradient at  $\alpha/\gamma$  interfaces can be influenced by both the diffusivity of manganese in ferrite and the mobility of the  $\alpha/\gamma$  interfaces [26,28]. It is worth emphasizing that the austenite growth is simultaneously accompanied with manganese partitioning into austenite, which stabilizes austenite down to room temperature. As a result of solute element partitioning across the  $\alpha/\gamma$  interfaces, austenite was largely enriched in manganese (~23wt%, Fig. 4(b)) but depleted in aluminum (~1.7wt% Fig. 4(c)). In practice, the diffusivity of manganese can be affected by the defects stored in the microstructure, for instance, dislocations generated by deformation or phase transformation. In this case, the pipe diffusion mechanism can strongly facilitate the diffusion of manganese in ferrite towards the  $\alpha/\gamma$  interfaces [26]. Therefore, a factor of five was applied in the present work to enhance the diffusivity of both manganese and aluminum in martensitic matrix compared with ferritic matrix. This factor seems to be a reasonable value, as indicated by the comparable reversion kinetics between the simulation and experiment (Fig. 3).

#### 4. Conclusions and remarks

In the present work, microstructure evolution in a medium-Mn alloy during intercritical annealing was simulated by the multiphase-field approach. The lamellar morphology of reversed austenite was successfully replicated by incorporating a faceted anisotropy model. The simulated austenite reversion kinetics reveals an excellent agreement with the experimental observations via *in situ* synchrotron high-energy X-ray diffraction. As a promising endeavor, the proposed approach is capable of modeling the microstructural morphology and austenite reversion kinetics in medium-Mn steels.

#### Acknowledgements

The authors gratefully acknowledge the financial support of the Deutsche Forschungsgemeinschaft (DFG) within the Collaborative Research Center (SFB) 761 ‘Steel-*ab initio*: Quantum mechanics guided design of new Fe-based materials’ and the project BL402/49-1. H.W. Luo is thankful for the financial supports from the National Natural Science Foundation of China (Nos. 51861135302 and 51831002). Dr. Bernd Böttger at ACCESS e.V. is acknowledged for the

helpful discussions. The synchrotron high-energy X-ray diffraction measurements were carried out at the Powder Diffraction and Total Scattering Beamline P02.1 of PETRA III at DESY (No. I-20181007), a member of the Helmholtz Association (HGF), which is gratefully acknowledged. Dr. Martin Etter at DESY is acknowledged for his support of acquiring HEXRD data.

**Open access** funding provided by Projekt DEAL.

**Open Access** This article is licensed under a Creative Commons Attribution 4.0 International License, which permits use, sharing, adaptation, distribution and reproduction in any medium or format, as long as you give appropriate credit to the original author(s) and the source, provide a link to the Creative Commons licence, and indicate if changes were made. The images or other third party material in this article are included in the article’s Creative Commons licence, unless indicated otherwise in a credit line to the material. If material is not included in the article’s Creative Commons licence and your intended use is not permitted by statutory regulation or exceeds the permitted use, you will need to obtain permission directly from the copyright holder. To view a copy of this licence, visit <http://creativecommons.org/licenses/by/4.0/>.

#### References

- [1] Y.K. Lee and J. Han, Current opinion in medium manganese steel, *Mater. Sci. Technol.*, 31(2015), No. 7, p. 843.
- [2] Y. Ma, Medium-manganese steels processed by austenite-reverted-transformation annealing for automotive applications, *Mater. Sci. Technol.*, 33(2017), No. 15, p. 1713.
- [3] B. Hu, H.W. Luo, F. Yang, and H. Dong, Recent progress in medium-Mn steels made with new designing strategies, a review, *J. Mater. Sci. Technol.*, 33(2017), No. 12, p. 1457.
- [4] D.K. Matlock and J.G. Speer, Processing opportunities for new advanced high-strength sheet steels, *Mater. Manuf. Processes*, 25(2010), No. 1-3, p. 7.
- [5] W. Bleck, F. Brühl, Y. Ma, and C. Sasse, Materials and processes for the third-generation advanced high-strength steels, *BHM Berg- Huttenmann. Monatsh.*, 164(2019), No. 11, p. 466.
- [6] L. Liu, B.B. He, and M.X. Huang, The role of transformation-induced plasticity in the development of advanced high strength steels, *Adv. Eng. Mater.*, 20(2018), No. 6, art. No. 1701083.
- [7] R.L. Miller, Ultrafine-grained microstructures and mechanical properties of alloy-steels, *Metall. Mater. Trans. B*, 3(1972), No. 4, p. 905.
- [8] S.W. Lee and B.C. De Cooman, Effect of the intercritical annealing temperature on the mechanical properties of 10 pct Mn multi-phase steel, *Metall. Mater. Trans. A*, 45(2014), No. 11, p. 5009.
- [9] P.J. Gibbs, E. De Moor, M.J. Merwin, B. Clausen, J.G. Speer, and D.K. Matlock, Austenite stability effects on tensile behavior of manganese-enriched-austenite transformation-induced plasticity steel, *Metall. Mater. Trans. A*, 42(2011), No. 12, p. 3691.
- [10] K. Steineder, D. Krizan, R. Schneider, C. Beal, and C. Sommitsch, On the microstructural characteristics influencing the yielding behavior of ultra-fine grained medium-Mn steels, *Acta*

- Mater.*, 139(2017), p. 39.
- [11] Y. Ma, W.W. Song, S.X. Zhou, A. Schwedt, and W. Bleck, Influence of intercritical annealing temperature on microstructure and mechanical properties of a cold-rolled medium-Mn steel, *Metals*, 8(2018), No. 5, p. 357.
- [12] H.W. Luo, J. Shi, C. Wang, W.Q. Cao, X.J. Sun, and H. Dong, Experimental and numerical analysis on formation of stable austenite during the intercritical annealing of 5Mn steel, *Acta Mater.*, 59(2011), No. 10, p. 4002.
- [13] C. Wang, J. Shi, C.Y. Wang, W.J. Hui, M.Q. Wang, H. Dong, and W.Q. Cao, Development of ultrafine lamellar ferrite and austenite duplex structure in 0.2C5Mn steel during ART-annealing, *ISIJ Int.*, 51(2011), No. 4, p. 651.
- [14] J. Han and Y.K. Lee, The effects of the heating rate on the reverse transformation mechanism and the phase stability of reverted austenite in medium Mn steels, *Acta Mater.*, 67(2014), p. 354.
- [15] T. Furukawa, H. Huang, and O. Matsumura, Effects of carbon content on mechanical properties of 5%Mn steels exhibiting transformation induced plasticity, *Mater. Sci. Technol.*, 10(1994), No. 11, p. 964.
- [16] Y. Ma, B.H. Sun, A. Schökel, W.W. Song, D. Ponge, D. Raabe, and W. Bleck, Phase boundary segregation-induced strengthening and discontinuous yielding in ultrafine-grained duplex medium-Mn steels, *Acta Mater.*, 200(2020), p. 389.
- [17] R. Schneider, K. Steineder, D. Krizan, and C. Sommitsch, Effect of the heat treatment on the microstructure and mechanical properties of medium-Mn-steels, *Mater. Sci. Technol.*, 35(2019), No. 17, p. 2045.
- [18] J. Han, S.J. Lee, C.Y. Lee, S. Lee, S.Y. Jo, and Y.K. Lee, The size effect of initial martensite constituents on the microstructure and tensile properties of intercritically annealed Fe–9Mn–0.05C steel, *Mater. Sci. Eng. A*, 633(2015), p. 9.
- [19] N. Moelans, B. Blanpain, and P. Wollants, An introduction to phase-field modeling of microstructure evolution, *Calphad*, 32(2008), No. 2, p. 268.
- [20] I. Steinbach, F. Pezzolla, B. Nestler, M. Seeßelberg, R. Prielier, G.J. Schmitz, and J. L.L. Rezende, A phase field concept for multiphase systems, *Physica D*, 94(1996), No. 3, p. 135.
- [21] B. Böttger, M. Apel, J. Eiken, P. Schaffnit, and I. Steinbach, Phase-field simulation of solidification and solid-state transformations in multicomponent steels, *Steel Res. Int.*, 79(2008), No. 8, p. 608.
- [22] M. Militzer, Phase field modeling of microstructure evolution in steels, *Curr. Opin. Solid State Mater. Sci.*, 15(2011), No. 3, p. 106.
- [23] J. Rudnizki, B. Böttger, U. Prael, and W. Bleck, Phase-field modeling of austenite formation from a ferrite plus pearlite microstructure during annealing of cold-rolled dual-phase steel, *Metall. Mater. Trans. A*, 42(2011), No. 8, p. 2516.
- [24] M. Toloui and M. Militzer, Phase field modeling of the simultaneous formation of bainite and ferrite in TRIP steel, *Acta Mater.*, 144(2018), p. 786.
- [25] W.W. Song, U. Prael, Y. Ma, and W. Bleck, Multiphase-field simulation of cementite precipitation during isothermal lower bainitic transformation, *Steel Res. Int.*, 89(2018), No. 8, art. No. 1800028.
- [26] O. Dmitrieva, D. Ponge, G. Inden, J. Millán, P. Choi, J. Sietsma, and D. Raabe, Chemical gradients across phase boundaries between martensite and austenite in steel studied by atom probe tomography and simulation, *Acta Mater.*, 59(2011), No. 1, p. 364.
- [27] H. Kamoutsi, E. Gioti, G.N. Haidemenopoulos, Z. Cai, and H. Ding, Kinetics of solute partitioning during intercritical annealing of a medium-Mn steel, *Metall. Mater. Trans. A*, 46(2015), No. 11, p. 4841.
- [28] J.J. Mueller, D.K. Matlock, J.G. Speer, and E. De Moor, Accelerated ferrite-to-austenite transformation during intercritical annealing of medium-manganese steels due to cold-rolling, *Metals*, 9(2019), No. 9, art. No. 926.
- [29] I. Steinbach, F. Pezzolla, and R. Prielier, Grain selection in faceted crystal growth using the phase field theory, [in] *Proceedings of the Modeling of Casting, Welding and Advanced Solidification Processes*, London, 1995, p. 695.
- [30] Y. Ma, *Processes, Microstructure, and Mechanical Properties of Cold-Rolled Medium-Mn Steel*, Verlagshaus Mainz GmbH Aachen, Aachen, 2020, p. 33.
- [31] A.C. Dippel, H.P. Liermann, J.T. Delitz, P. Walter, H. Schulte-Schrepping, O.H. Seeck, and H. Franz, Beamline P02.1 at PETRA III for high-resolution and high-energy powder diffraction, *J. Synchrotron Radiat.*, 22(2015), No. 3, p. 675.
- [32] A. Dutta, D. Ponge, S. Sandlöbes, and D. Raabe, Strain partitioning and strain localization in medium manganese steels measured by *in situ* microscopic digital image correlation, *Materialia*, 5(2019), art. No. 100252.
- [33] A.P. Hammersley, FIT2D: A multi-purpose data reduction, analysis and visualization program, *J. Appl. Crystallogr.*, 49(2016), No. 2, p. 646.
- [34] L. Lutterotti, Total pattern fitting for the combined size–strain–stress–texture determination in thin film diffraction, *Nucl. Instrum. Methods Phys. Res., Sect. B*, 268(2010), No. 3–4, p. 334.
- [35] Y. Ma, W.W. Song, and W. Bleck, Investigation of the microstructure evolution in a Fe–17Mn–1.5Al–0.3C steel via *in situ* synchrotron X-ray diffraction during a tensile test, *Materials*, 10(2017), No. 10, art. No. 1129.